Fragmentation cross sections of 600 MeV/nucleon ^{20}Ne on elemental targets

C. Zeitlin,[1] A. Fukumura,[2] L. Heilbronn,[1] Y. Iwata,[2] J. Miller,[1] and T. Murakami[2]
[1]*Lawrence Berkeley National Laboratory, Berkeley, California 94720*
[2]*National Institute of Radiological Sciences, Chiba, Japan*

Charge-changing and fragment production cross sections have been obtained for interactions of a 600 MeV/nucleon neon beam in H, C, Al, Cu, Sn, Ta, and Pb targets. The H target results were obtained using a polyethylene target and subtracting the cross sections obtained with the carbon target. At 600 MeV/nucleon, the angular distributions of the fragments are strongly forward peaked, and consequently the spectra seen in the detectors with the largest angular acceptance—corresponding to a forward cone with half angle 7°—show obvious fragment peaks only for charges 5 through 9. No clear peaks are seen below charge 5 in the large-acceptance detectors, but spectra from detectors subtending smaller angular acceptances show peaks for all fragment species, and additional identifiable peaks from events with between two and four fragments in coincidence. Production cross sections for all fragment species are reported here and, where possible, compared to earlier measurements and to the predictions of three model calculations (Nucfrg2, Qmsfrg, and an empirical parametrization that is tuned for higher-mass beams). The cross sections for fragments of charge 5 and below have not been previously reported. Also, the charge-changing cross sections are compared to earlier measurements and to Nucfrg2 and the Bradt-Peters model.

I. INTRODUCTION

Nuclear fragmentation has been extensively studied for a number of years for the insight it can provide into basic nuclear physics. More recently, applications such as hadron therapy and radiation risk assessment for personnel on space missions [1] have spurred measurements with specific ions. Lighter nuclei such as neon are of interest for several reasons related to their fragmentation properties. The ionization energy loss of neon ions—100 times greater than that of protons of the same velocity—makes them desirable for some types of hadron radiotherapy [2]. However, nuclear fragmentation affects the dose vs depth profile and must be taken into account in treatment planning. In space, the damage that heavy ions in the galactic cosmic radiation (GCR) can produce in healthy cells and tissue may have long-term implications for astronaut health [3]. The flux of ions in free space is well known [4], but fragmentation in spacecraft walls, equipment, etc., modifies the incident radiation field. Uncertainties in fragmentation cross sections propagate as fragments build up due to secondary and higher-order collisions, and may lead to large uncertainties in calculations of radiation dose and dose equivalent [5]. The principles of radiation protection dictate that spacecraft designers and mission planners err on the side of caution, so that these large uncertainties may impose unnecessary limitations on allowed mission duration, or make the cost of shielding prohibitively high. Detailed knowledge of the fragmentation of neon and other prominent ions at characteristic GCR energies[1] is required to accurately calculate dose and dose equivalent inside a shielded environment, including the self-shielding effect of tissue.

In previous works, we reported on fragmentation measurements with iron ions [6,7], which are the heaviest ions present in significant numbers in the GCR. Lighter ions, such as neon, are of interest both as significant components of the GCR and because their fragmentation cross sections may help elucidate nuclear structure effects that might be obscured in the complicated final states produced by interactions of heavier ions. Further, the production cross sections for the lightest fragment species, previously unreported, may be particularly useful in distinguishing between models. Here we present the first report on a series of measurements at the Heavy Ion Medical Accelerator in Chiba (HIMAC) at the National Institute for Radiological Sciences, Chiba, Japan, performed in February 1998, using a beam of ^{20}Ne ions with 600 MeV/nucleon kinetic energy at extraction from the accelerator. The actual energy at the target entrance point is calculated to be 585 MeV/nucleon, taking account of materials between the end of the vacuum line and the target.

II. EXPERIMENTAL SETUP

A 0° fragmentation experiment, similar to others performed by our group at the Lawrence Berkeley National Laboratory (LBNL) Bevalac [6] and the Brookhaven National Laboratory's Alternating Gradient Synchrotron [7] was carried out at the HIMAC. The experiments use fully

[1]As illustrated in Ref. [4], the kinetic energy spectra of the prominent heavy ions in the GCR have broad peaks in the range from 100 to 1000 MeV/nucleon.

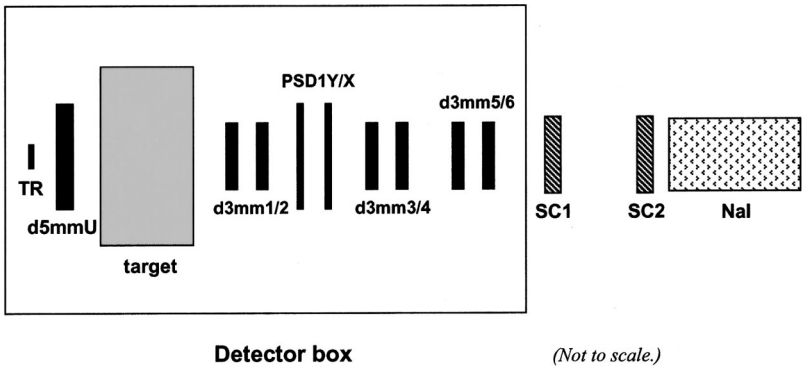

FIG. 1. Schematic representation of detectors on the beamline. Beam is incident from the left. The detector positions relative to target center, their active radii and acceptance angles are given in Table I.

depleted silicon detectors to measure deposited energy (ΔE), providing particle identification. Just downstream of the vacuum exit window, we placed the ''detector box'' [8], which provides holders for 16 detectors, at 2 cm intervals along the beam direction. The side placed in the beam holds circular silicon detectors; the other side holds electronics boards with charge-sensitive preamplifiers and on-board calibration circuitry. The preamplifier output signals were used as inputs to NIM shaping amplifiers in the counting room (located about 100 m from the beamline). The shaping amplifier outputs were digitized in 12-bit CAMAC analog-to-digital converters (ADC's). The event rate was typically 400–500 events/sec during the 0.6-sec-long spill, with data acquisition lifetime in the 65–80 % range. About 3×10^5 events were obtained for each target. The targets presented between 7.5% and 18% of an interaction length to the beam.

Figure 1 shows a schematic representation of the detector arrangement for this run. The first element in the silicon detector stack (''TR'') was a 300-μm-thick trigger detector with an active area of 50 mm^2, placed in the most-upstream position in the detector box. A 5-mm-thick lithium-drifted detector with an active area of about 1400 mm^2, referred to as d5mmU, was placed 2 cm downstream of TR. The event trigger was a coincidence of hits in these two detectors, with thresholds set to about 80% of the expected pulse height from a beam ion. Targets were cut to fit inside the detector box, and when present were inserted so that their centers were 3 cm downstream from d5mmU. Downstream of the target location, six 3-mm-thick lithium-drifted silicon detectors, with active areas of 400 mm^2, were placed as indicated in Table I. These were the main particle identifiers; we refer to them as d3mm1, d3mm2, etc. In each pair of detectors (d3mm1/2, d3mm3/4, d3mm5/6), only 2 cm separated the two, so that each subtended very nearly the same solid angle as seen from the center of the target. For d3mm 3, 4, 5, and 6, two readout channels were implemented, one in which the entire ΔE spectrum could be seen, and a high-gain channel that provided higher resolution for fragment charges 3 and below.

The target materials and depths, along with the calculated energies in MeV/nucleon at target center in parentheses, were as follows: 3.99 g cm^{-2} carbon (563), 2.89 g cm^{-2} polyethylene (566), 3.24 g cm^{-2} aluminum (569), 7.17 g cm^{-2} copper (555), 5.97 g cm^{-2} tin (563), 10.0 g cm^{-2} tantalum (550), and 10.2 g cm^{-2} lead (551).

Pulser calibration data were taken at the beginning and end of the run. An on-board system, running under computer control, injects a sequence of known charges into the front end of the preamplifier circuit, testing the response of the entire electronics chain. Off-line analysis of these data yielded the scale factors that relate pulse height to ΔE, using the standard assumption that one electron/hole pair is created in silicon for each 3.6 eV of ΔE. The calibration data show a highly linear response over the highest 98% of the range encountered in the experiment. While beam data were being taken, a low-rate random trigger was fired so that pedestals could be monitored. Pedestals and calibration peaks were found to be stable to within two ADC channels over the course of the run.

Position-sensitive detectors [9], referred to as PSD's were placed in between d3mm2 and d3mm3. These units have active areas of 1400 mm^2, and each has two output signals from which one can determine position in one coordinate via charge division. The more-upstream detector was oriented to measure y, and the more-downstream detector measured x ($+z$ is the direction of the incident beam). Each PSD provides a third signal, proportional to the total charge collected (i.e., a ΔE signal). Target-out data show that the beam spot had a full width at half maximum of approximately 2.5 mm

TABLE I. Detector types, depths, radii, distances from target center, and acceptance angles. For the plastic scintillators, the angles are approximated by treating the detector areas as equivalent circular areas. The actual active radii of the silicon detectors vary slightly; 1.15 and 2.0 cm are the approximate averages for the 3-mm-thick units and PSD's, respectively.

Detector	Type, thickness (mm)	Active radius (cm)	Dist. to target (cm)	Acceptance Angle (deg.)
d3mm1	Si, 3.04	1.15	7.0	9.3
d3mm2	Si, 3.08	1.15	9.0	7.3
PSD1Y	Si, 1.03	2.0	11.0	10.3
PSD1X	Si, 1.01	2.0	13.0	8.7
d3mm3	Si, 3.06	1.15	15.0	4.4
d3mm4	Si, 3.08	1.15	17.0	3.9
d3mm5	Si, 3.06	1.15	23.0	2.9
d3mm6	Si, 3.08	1.15	25.0	2.6
Scint1	plastic, 5.0	square 10×10	126.6	2.6 (approx.)
Scint2	plastic, 5.0	square 10×10	630	0.51 (approx.)
NaI	NaI, 127	6.35	636 (center)	0.57

in both x and y, considerably smaller than the 8 mm diameter of the trigger detector. The beam spot was centered within 1.5 mm of the nominal centerline and had very small divergence ($\theta \approx 2.2$ mrad, see Sec. VIII).

Two 5-mm-thick plastic scintillators, referred to as Scint1 and Scint2, and a NaI crystal of 12.7 cm depth were also placed on the beamline downstream of the detector box. Pulse heights for these detectors were digitized in 11-bit ADC's, and timing information from the scintillators was digitized via a time-to-analog converter and another 11-bit ADC channel. Scint1 was placed so as to have approximately the same acceptance as d3mm6, and Scint2 was placed as far downstream as possible to maximize the flight path for the time-of-flight measurement. The NaI crystal was deep enough to stop primaries and most fragments, giving a measurement of total energy. Data from these detectors are, for the most part, not used in the present analysis, but the pulse height data from Scint2 are useful in categorizing light fragment events.

The acceptance angle of a downstream detector is defined to be the half-angle of the forward cone it subtends, as seen from a point exactly on the beam centerline and at the middle of the target. With an infinitesimal beam diameter, a plot of acceptance vs angle would be a step function. In practice, because the beam spot has a finite diameter, such plots deviate slightly from step functions. Beam divergence, Coulomb scattering, and nuclear scattering further complicate matters; when we refer to acceptances, one should keep these factors in mind. Table I lists the positions, areas, and nominal acceptance angles of the detectors used in this experiment. The Monte Carlo model used to determine the acceptances is described in detail in the Appendix.

III. DATA ANALYSIS

In the off-line analysis, we reduce the sample to events in which a single neon ion was present upstream of the target. The sample is obtained by selecting events within about two standard deviations of the neon peak in both TR and d5mmU. This removes events in which the incident ion was of a species other than neon, and also removes the vast majority of events where an incident neon ion underwent a charge-changing interaction in TR or d5mmU.

To identify particles downstream of the target, we use a method based on cuts made in scatter plots of ΔE in neighboring detectors (d3mm2 vs 1, 4 vs 3, and 6 vs 5), similar to that used in Ref. [7]. Clear signals are seen for charges 5 through 10, and, as we will show, many combinations of lighter fragments can be distinguished in the small-acceptance detectors. Figure 2 shows a typical scatter plot of ΔE in d3mm2 vs ΔE in d3mm1; well-correlated events lie along the densely populated 45° line, outlined by the contour used to select good events. Near the cluster of Ne events, the contour is drawn to exclude events that could end up in the charge 9 (F) peak when the d3mm1 and d3mm2 signals are summed. The cut is deliberately left loose at the low end in order to retain events in which d3mm1 was hit by one or more fragments that missed d3mm2, owing to its smaller acceptance.

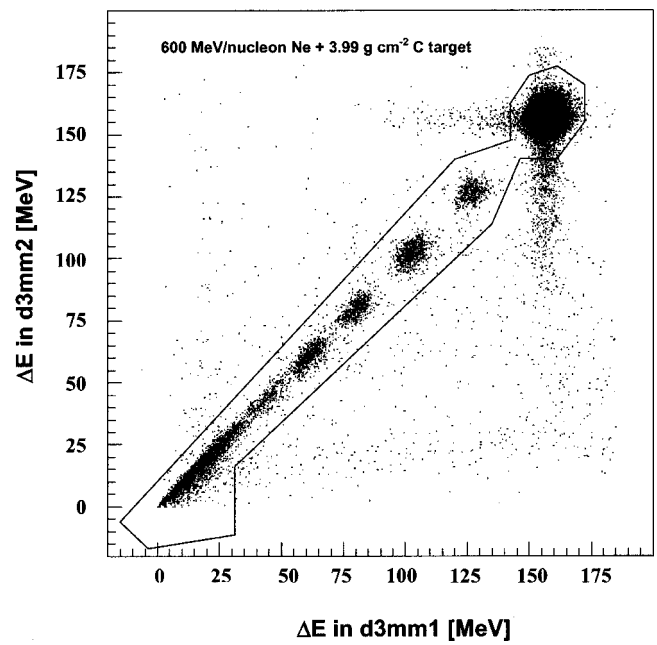

FIG. 2. Scatter plot of ΔE in d3mm2 vs ΔE in d3mm1, showing a typical cut contour used to select events with well-correlated signals in the two detectors; data are from the run with the carbon target.

Figure 2 shows a band of events with ΔE consistent with Ne in d3mm2 but lower than expected for Ne in d3mm1. These are events where a primary ion hits both detectors but its energy deposition is not fully registered in d3mm1—about 0.5% of events with neon ions fall into this region. There is also a band of events with a fully registered Ne ion in d3mm1, but lower-than-Ne energy deposition in d3mm2. Two indistinguishable types of events contribute here: those in which a Ne ion undergoes a charge-changing nuclear interaction in d3mm2, and events where the Ne traverses d3mm2 but less than nominal energy was registered. To determine cross sections, we select only the events in which d3mm1 and d3mm2 have well-correlated ΔE as defined by the cut contour. A histogram of the summed ΔE in d3mm1 and d3mm2 is made, as shown in Fig. 3. We refer to this sum as ΔE_{12}. A large peak of neon ions stands out, and at least five other peaks are visible. A Gaussian is fit to the central

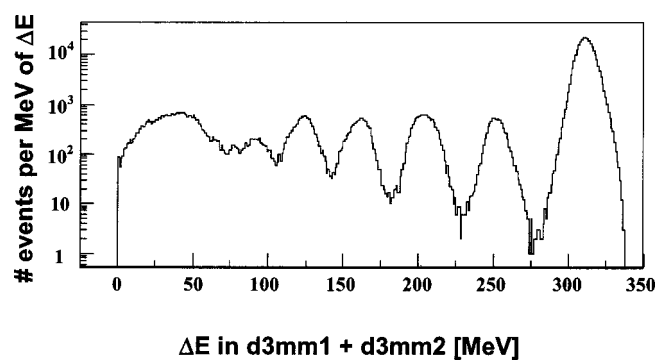

FIG. 3. Histogram of ΔE summed over d3mm1 and d3mm2, for the events selected by the correlation cut shown in Fig. 2.

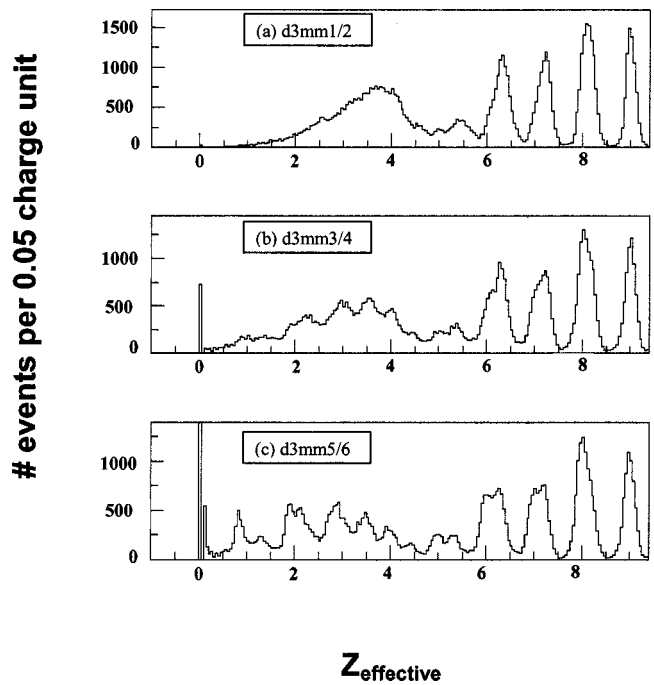

FIG. 4. Histrograms of ΔE's summed over detector pairs and scaled to ''Z,'' according to Eq. (1). The Ne peaks have been excluded from the histograms in order to emphasize the changes in fragment spectra seen as detector acceptance decreases. In (c), the vertical scale has been limited to a peak of 1400 events per 0.05 units of Z to make the fragment peaks more visible; the pedestal peak in this data set contains about 2100 events. These data were obtained with the CH_2 target.

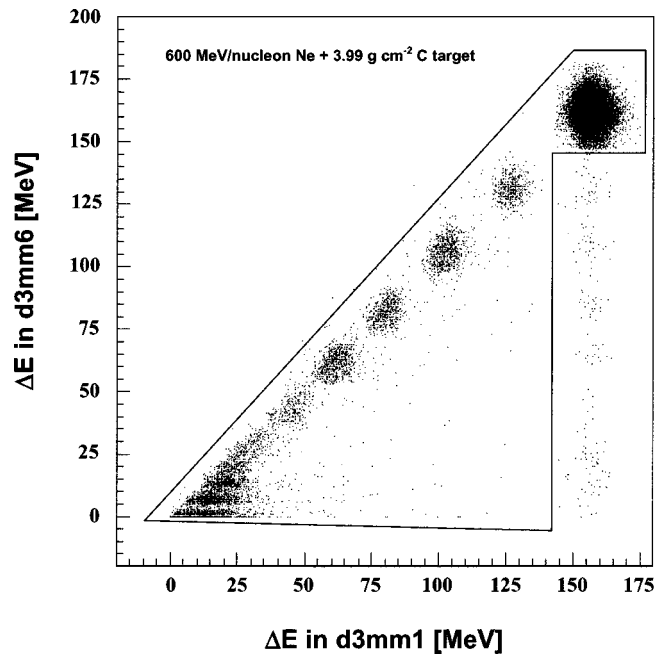

FIG. 5. Scatter plot of ΔE in d3mm6 vs ΔE in d3mm1, again from the run with the carbon target. The plot shows a typical cut contour used to exclude from events in which a Ne ion has a charge-changing interaction in the silicon stack. Events in which some light fragments hit d3mm1 but miss d3mm6 are visible as bands in the lower left-hand corner of the plot.

region of the neon peak to determine ΔE_{12}(Ne), i.e., the peak value of the summed ΔE. With the same event sample, we make a histogram of the quantity Z_{12}, the effective charge detected, defined to be

$$Z_{12} = 10\sqrt{\Delta E_{12}/\Delta E_{12}(\mathrm{Ne})}\cdot \tag{1}$$

Using the neon peak to determine the Z scale implicitly assumes that the fragments are at or near the velocity of the primary ions. As can be seen in Fig. 4(a), this works well for the F and O fragments, as obvious peaks are seen at Z_{12} of 9 and 8. Peaks for lighter fragments, N, C, and B, are shifted noticeably to the right of the nominal integer values where one would naively expect them to appear. This is due to the presence of additional fragments, which deposit their energy in the detectors coincident with the deposition from the leading (highest Z) fragment. Assuming all fragments are at the beam velocity, the effective detected charge is given by

$$Z_{\mathrm{eff}} = \sqrt{\sum Z_i^2}, \tag{2}$$

where the sum inside the square root runs over all fragments within the acceptance. If the leading fragment is near the beam charge, it dominates the sum and the effect of lighter fragments in the event will not be discernible. For fragments further from the beam charge, the influence of nonleading light fragments becomes more significant.

Events in which there is no fragment with at least half the beam charge fall into the broad hump of events below $Z_{12} \approx 4.5$, where little or no structure is discernible. Events with Z_{12} below 0.5 are considered to be pedestals and are counted in a separate category.

The analysis procedure used for d3mm 1 and 2 is repeated for the d3mm 3 and 4 detector pair, and again for d3mm 5 and 6. In the d3mm3/4 analysis, the previous cuts are retained and three additional cuts are made. First, a correlation cut is made in the scatter plot of ΔE in PSD1Y vs ΔE in PSD1X, the primary purpose being to remove events in which there is a charge-changing interaction of either primaries or fragments in the detectors. Second, a correlation cut is made on the signals in d3mm 3 and 4, analogous to the one made in the d3mm1/2 analysis (illustrated in Fig. 2). Third, a scatter plot is made with ΔE in the d3mm4 plotted against ΔE in d3mm1. A small number of events appear in which there is fragmentation of a Ne ion in the silicon stack; these are easily removed with a graphical cut, similar to the one discussed below for d3mm6 vs d3mm1 and shown in Fig. 5.

In the d3mm5/6 analysis, events are required to have passed all of the cuts described so far, and two additional cuts, one requiring good correlation between d3mm5 and d3mm6, the other made in the d3mm6 vs d3mm1 plot to remove any remaining fragments created by interactions of Ne in the detector stack. The latter is illustrated in Fig. 5. This plot also shows, in the lower left-hand corner, distinct clusters of events with multiple fragments in d3mm1 but only a single fragment in d3mm6. These are especially prevalent when there is no leading fragment with charge 5 or

higher, corresponding to the featureless region of Fig. 4(a).

In the analyses using the downstream silicon detectors, we generate histograms of Z_{34} and Z_{56}, analogous to Z_{12}. Again, these are ''effective'' charges, since events with multiple fragments are included. Typical spectra are shown in Figs. 4(b) and 4(c) for d3mm3/4 and d3mm5/6, respectively. The light fragment peaks become much clearer as the angular acceptance decreases, since the detected fragment multiplicity decreases. This effect is governed by the fragment transverse momentum distributions, which broaden significantly with decreasing mass [10]. Deeper in the stack, many light fragments are outside the acceptance, reducing the number of combinations of fragment final states that can produce a particular Z_{eff}. Also, compared to the d3mm1/2 data, higher fractions of events with no charged fragments are seen in the d3mm3/4 and d3mm5/6 data.

The spectra from the downstream detectors allow us to determine cross sections for all fragments, and to compare the cross sections for charges 5–9 at large acceptance to those obtained with smaller acceptance. In the small-acceptance spectra, several peaks appear at noninteger locations, as seen most readily in Z_{56} [Fig. 4(c)]. Several features in Fig. 4(c) were not visible in the Z_{12} histogram. The first of these is a doubling of the peak near $Z_{56}=6$. The higher-Z peak, near 6.25, is likely due to events with one carbon and one helium ion detected in coincidence, or to a carbon ion in coincidence with three or four protons; the peak near 6.0 is likely due to carbon without any lighter ions in the acceptance (or perhaps with one or two protons that have no discernible effect on Z_{56}). The same effect is seen in the Z_{34} histogram, where the $Z_{34}\approx 6.25$ peak is the more populated of the two. The relative decrease of the number of events in the $Z\approx 6.25$ peak at smaller acceptance is consistent with the presence of nonleading light fragments. Further evidence for this comes from Fig. 8, which shows a considerable number of charge 6 events with nonleading He fragments (see Sec. VIII). The doubling of the peak is seen, with varying degrees of statistical significance and resolution, in all data sets. We have chosen to present the spectrum from the CH_2 target run, as it shows the effect clearly.

Peaks in the Z_{56} spectrum that were not seen in Z_{12} are found near 5.4, 5, 4.4, 4, 3.5, 2.9, 2.2, 1.9, 1.3, and 0.9. The peaks at 5 and 5.4 probably correspond to B and (B+He), respectively; those near 4 and 4.4 have multiple contributions (see Sec. VIII). The peak near 3.5 is dominated by events with three He fragments in coincidence (these are counted in a separate category for the cross-section determination). The peak near 2.9 contains a combination of events with a leading Li fragment and events with two He fragments; the signatures of the two types of events are indistinguishable in the silicon detectors, hence we refer to these as ''charge 3'' events. (In Sec. VIII, we use Scint2 data to set upper limits on the percentage of these events containing a Li fragment.) The remaining peaks, containing events with leading H and He fragments, are discussed in Sec. VII.

When we sort events to determine the fragment production cross section for each species, events are categorized by the leading (largest) fragment Z, regardless of the presence or absence of additional, lighter fragments. For instance, events in both the $Z\approx 6$ and $Z\approx 6.25$ peaks are counted as carbon fragment events.

In the Z_{34} and Z_{56} spectra, the light-fragment peaks are slightly shifted to the left of their nominal values. There are two contributions to these shifts: one is a kinematic effect, and the other is due to nonlinearity in the ADC's at the extreme low end (relevant only for protons). The kinematic effect arises because lighter fragments lose considerably less velocity in traversing the detector stack than do primaries or heavy fragments. The Z scaling method, which assumes all particles are at the same velocity, begins to break down—the lighter fragments are at slightly higher velocity than the heavier particles. This leads to a relative decrease in deposited energy and thus a small decrease in Z_{34} or Z_{56}.

Because the analysis depends on graphical cuts made interactively using the CERN library package PAW [11], the results are prone to variations arising from the small degree of subjectivity involved in drawing cut contours. Efforts are made to perform analysis as consistently as possible on all data sets, and, in extracting results, we take into account the systematic errors arising from this method.

IV. RESULTS: CHARGE-CHANGING CROSS SECTIONS

Once the histogram of Z_{12} has been obtained for a particular target, the numbers of events in the different categories are determined simply by counting directly from the histogram. For the d3mm1/2 analysis, we define eight categories: $Z=10$, 9, 8, 7, 6, 5, 1 to 4, and 0. The numbers in each category are counted by summing over the bins deemed to correspond to a particular charge. The valleys between the peaks contain very few events for charges 6 through 10, and, as a result, ambiguities in picking which bins to assign to a particular charge category contribute uncertainties that are much smaller than those due to counting statistics. However, for the two peaks assumed to be due to charge 5 fragments ($Z_{12}\approx 5.0$ and $Z_{12}\approx 5.4$), the separation from neighboring peaks is less clear, particularly on the low end of the peak near 5.0. In this case (and in similar cases in the analysis of Z_{34} and Z_{56} spectra, discussed below), we take the uncertainty in the number of charge 5 events to be the quadrature sum of the statistical uncertainty ($\sqrt{N}$) and reasonable variations in the choice of bins.

The numbers of events determine the charge-changing and fragment production cross sections, although several corrections to the raw numbers are needed. First, one must take account of events lost due to charge-changing nuclear interactions in the detector, which are greatest for the primary ion species and decrease as fragment Z (and A) decrease. We use a form [12] of the geometric cross sections $\sigma(A_{\mathrm{proj}})$ to determine the survival of ions of a given species through a depth of silicon d. Numbers of events are then corrected according to

$$N_{\mathrm{corr}}=\frac{N_{\mathrm{meas}}}{e^{-dN_A\rho\sigma(A_{\mathrm{proj}})/A}}, \tag{3}$$

TABLE II. Charge-changing cross sections in millibarns for the 600 MeV/nucleon Ne beam incident on various target materials as determined by the present experiment (top row), three theoretical models described in the text, Chen *et al.* [15] and Webber, Kish, and Schrier [16] at energies very close to those in the present experiment, and Fukumura *et al.* [17], at somewhat lower energies than in this experiment. The average energies in MeV/nucleon for the Fukumura *et al.* data are shown in parentheses beneath the cross sections.

σ_{cc} (mb) from:	H	C	Al	Cu	Sn	Ta	Pb
Present expt.	299±9	987±29	1354±41	1981±59	2537±76	3179±95	3396±102
Nucfrg2	331	1000	1374	1979	2624	3210	3429
*B-P*1		997	1366	1983	2650	3256	3483
*B-P*2		969	1329	1933	2587	3182	3406
Chen *et al.* [15], ^{22}Ne	327±9						
Webber, Kish, and Schrier [16]	319±8	980±10					
Fukumura *et al.* [17]	272±50 (233)	1011±40 (267)	1328±200 (272)	2267±200 (313)			

where N_A is Avogadro's number, and ρ and A refer to silicon. We take A_{proj} to be that of the most abundant naturally occurring isotope of a given species. For Ne, corrections due to interactions in d3mm1–2 are less than 5%, and are smaller for lighter ion species.[2] For the $Z=1$ to 4 category, no correction is made, in accordance with the choice of cut contour as illustrated in Fig. 2 (which retains events in which a light fragment could interact in the stack). Also, no correction is made for the ''$Z=0$'' category, for obvious reasons.

In the following, we define the fraction f_z of events in a given category to be the number of those events divided by the total number of events in the sample, after applying the corrections for losses in the silicon stack. The next correction accounts for interactions in materials other than the target and stack, e.g., in the air gaps between detectors and in detector dead layers. The probability of fragmentation in these materials is determined using target-out data, where the fraction of neon events is near 0.99 and the remaining 1% of events are distributed among the various fragment categories. For the target-in runs, the fraction of corrected events with a surviving primary is always greater than the fraction in the raw data, according to

$$f_{z=10}=\frac{N(Z=10)/N_{\text{pass}}}{N^{\text{t-o}}(Z=10)/N^{\text{t-o}}_{\text{pass}}}, \tag{4}$$

where the N are as defined in equation (3) (i.e., corrected for losses in the stack), the superscript ''t-o'' indicates numbers from the target-out data, and the subscript ''pass'' indicates the total number of events in a given sample after all cuts have been applied. For the fragment categories, the fractions are decreased by the target-out correction, since the interactions in the detector stack produce a small number of background fragments. The corrected fraction is given by

$$f_z=\frac{N(Z)}{N_{\text{pass}}}-\left(\frac{N^{\text{t-o}}(Z)}{N^{\text{t-o}}_{\text{pass}}}\right)f_{z=10}. \tag{5}$$

With these definitions, the sum over all f_z is exactly equal to 1. The charge-changing cross section is given by

$$\sigma_{\text{cc}}=\frac{A_{\text{tgt}}}{N_A\rho x}\ln(f_{z=10}). \tag{6}$$

In our other analyses using analogous techniques [7], two or three depths of material were used for each elemental target, and the RMS spread in the charge-changing cross sections for each material was typically about 3% of the average value. This is substantially greater than can be accounted for by the statistical errors, hence we attribute the spread to systematic errors in the data analysis procedure. Due to limitations of the ion source at the accelerator, the Ne beam run was shorter than our usual runs and we were only able to use one depth per target material. To be conservative in estimating errors, we apply the 3% systematic error seen in other data sets.

Table II shows our results for σ_{cc}, along with model calculations. The result for the H target was obtained using the carbon and polyethylene (CH_2) target cross sections according to $\sigma_{\text{cc}}(\text{H})=0.5[\sigma_{\text{cc}}(\text{CH}_2)-\sigma_{\text{cc}}(\text{C})]$. The first set of comparisons we make is to the semiempirical nuclear fragmentation model Nucfrg2 [13]. The output from the Nucfrg2 code is sufficiently detailed to allow us to subtract the neutron-stripping cross sections from the total absorption cross sections to yield the values shown. Excellent agreement with the data is seen: For all targets except H and Sn, the model predictions are within the 3% uncertainties on the cross sections, and the discrepancy for Sn is 3.4%. Next, we compare to ''*B-P*1,'' a simple geometric cross section calculation based on the Bradt-Peters [14] form (which is explicitly not intended to apply to H targets). The model contains two free parameters, the nucleon radius r_0 and the overlap parameter b; there are theoretical uncertainties asso-

[2]There are small uncertainties (less than 1%) in the corrections calculated in equation (3) due to uncertainties in the actual isotopic distributions of the fragments. Since the corrections themselves are 5% or less, the total error from this source is <0.05% in the d3mm1/2 results.

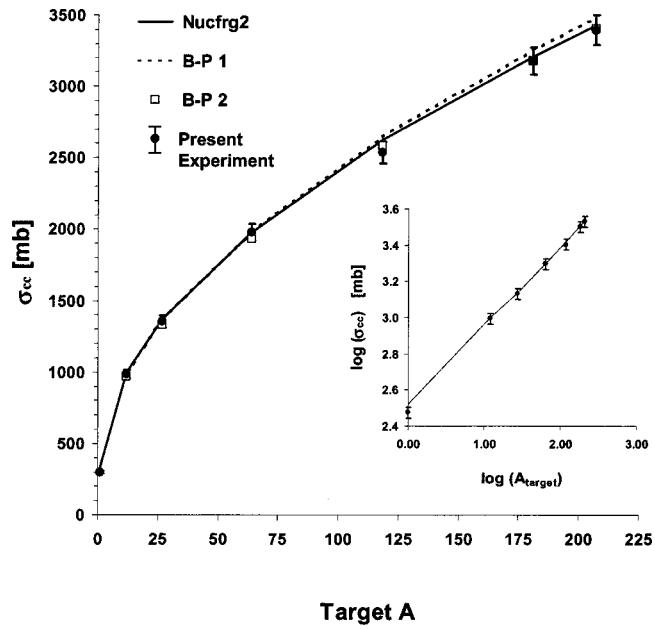

FIG. 6. Charge-changing cross sections as a function of target mass. Model predictions from Nucfrg2 are shown, along with the Bradt-Peters form with two choices of parameters, as explained in the text. The inset figure shows the data and the Nucfrg2 result on logarithmic scales.

ciated with both, and strong correlation between the two. The experimentally determined parameters reported by Chen *et al.* [15] are used in ''B-$P1$'' in Table II; the calculations reproduce the measured σ_{cc} for C, Al, and Cu targets to better than 1% in each case. For the heavier targets, the calculations are consistently higher than the data, although within the data uncertainties (except for Sn). In ''B-$P2$,'' we slightly adjust these parameters to better fit the data at large target masses, with the result that the predictions for lower target masses are below the data by about 2%. The values of r_0 and b from Ref. [15] are 1.35 fm and 0.83, respectively; our adjusted values are 1.34 fm and 0.86. In Fig. 6, we graphically illustrate these comparisons; the figure shows the charge-changing cross section as a function of target mass (points with error bars) and curves corresponding to these three models. The inset figure shows the same data on logarithmic scales, which clearly demonstrates the power-law dependence for targets heavier than hydrogen. Also shown in the inset is a line representing the Nucfrg2 predictions.

The charge-changing cross section for ^{20}Ne on hydrogen at 599 MeV/nucleon was reported by Webber, Kish, and Schrier [16], and Chen *et al.* [15] reported on ^{22}Ne on hydrogen at 581 MeV/nucleon; these results are shown in Table II. The two earlier experiments agree with each other within uncertainties, and both are within about 6% of the value obtained here. However, we expect from geometric models that the ^{22}Ne charge-changing cross section should be 5–10 % larger than that for ^{20}Ne, so that in fact the two earlier results are not in particularly good agreement. As we will discuss below, when one accounts for the increased F cross section in the ^{22}Ne data, the remaining charge-changing cross section is in excellent agreement with the present measurement. Webber, Kish, and Schrier also measured the charge-changing cross section for ^{20}Ne on C; their result agrees with ours to within 1%. Several of the same target materials used here were also used by Fukumura *et al.* [17] in a measurement of charge-changing cross sections at somewhat lower average energy; these are shown in the last row of Table II. In all cases, our results are seen to agree with the earlier measurements, within the errors.

V. FRAGMENT PRODUCTION CROSS SECTIONS FOR CHARGES 5 TO 9

The formalism for obtaining the charge-changing cross section is easily extended to determine the partial cross sections for the production of individual fragment species. Given the corrected fractions for the various fragment species as per equation (5), and the charge-changing cross section as per equation (6), the production cross section for a fragment species with charge Z is given by

$$\sigma_Z = \frac{f_Z}{\sum_{Z<Z_{\rm prim}} f_Z} \sigma_{\rm cc}(1+\delta_z), \tag{7}$$

where the sum in the denominator runs over all fragments and δ_Z (which can take on both positive and negative values) is the ''target correction'' discussed below, needed to account for secondary and higher-generation reactions in the target. Target corrections aside, the sum of all fragment production cross sections defined in this way exactly equals the charge-changing cross section.

Fragment production cross sections must be corrected for secondary and higher-order interactions in the target. For fragments near the beam charge, these interactions result in a net loss and the correction term $(1+\delta_Z)$ in Eq. (7) will be greater than 1. For light fragments, ''feed down'' from higher-charge fragments can be more significant than the losses due to interactions, and $(1+\delta_Z)$ can take on values less than 1. With thin targets, these are small corrections, but because they depend on unknown cross sections, one must use a model at this stage. In estimating the corrections, we have chosen to use the cross sections from Nucfrg2, as discussed in detail in Ref. [7]. The largest correction for any single fragment cross section is 9% (for F with the CH_2 target); more typically, they are in the 2–5 % range. We estimate the uncertainties on the correction factors to contribute a systematic error of no more than 3% to each cross section.

Table III shows our results using the d3mm1/2 detector pair, for fragment charges from 5 to 9 for H, C, Al, Cu, Sn, and Pb targets. We also show cross sections summed over charges 1–4, and for pedestal events, in which no forward-going charged fragments are within the detector acceptance. The error on the charge-changing cross sections, which is dominated by the assumed 3% systematic error, propagates into the fragment-production cross sections. Added in quadrature to the $\leqslant$3% uncertainty arising from the target correction factors, we estimate the total systematic uncertainty on each cross section to be 4% or less. This is added in quadrature to the statistical error (and, for charge 5, the error

TABLE III. Fragment production cross sections in millibarns for $5<Z<9$, charges 1–4 combined, and pedestals, using the d3mm1/d3mm2 detector pair. Comparisons to the results of Webber, Kish, and Schrier [16] for carbon and hydrogen targets, and to the ^{22}Ne data of Knott *et al.* [18] for a hydrogen target, are also shown.

Z_{frag}	σ (mb) from:	H	C	Al	Cu	Sn	Ta	Pb
9	This expt.	52±4	83±4	111±5	144±7	177±9	215±10	235±11
	Ref. [16]	49±3	92±2					
	^{22}Ne [18]	79±5						
8	This expt.	71±6	132±6	159±7	202±9	236±12	280±13	300±14
	Ref. [16]	75±4	151±2					
	^{22}Ne [18]	67±2						
7	This expt.	52±5	101±4	123±6	155±7	178±9	213±10	221±11
	Ref. [16]	60±3	111±3					
	^{22}Ne [18]	56±2						
6	This expt.	54±5	124±5	151±7	198±9	239±11	255±12	271±13
	Ref. [16]	59±3	126±4					
	^{22}Ne [18]	48±3						
5	This expt.	22±4	66±3	78±4	99±7	120±7	144±10	153±10
	Ref. [16]	14±2	53±3					
	^{22}Ne [18]	23±3						
1–4	This expt.	61±16	494±20	743±30	1167±48	1489±64	1914±86	1981±87
pedestal	This expt.	0±2	0±2	7±2	50±9	128±21	200±36	279±35

associated with choosing which bins to count as charge 5 in the Z_{12} plot); in almost all cases, the systematic error dominates the sum.

Acceptance calculations indicate that the acceptance for fragments with charges from 5 to 9 is at least 99% in the d3mm 1/2 pair, provided one uses physically reasonable values (80–120 MeV/c) of the parameter σ_0 that controls the widths of the transverse momentum distributions. Hence it is not necessary to make acceptance corrections to these cross sections. See Sec. VII for a more in-depth discussion of acceptance issues.

For the C and CH_2 targets, our cross sections are directly comparable to those from Webber, Kish, and Schrier [16], which are also shown in Table III for charges 6 through 9, the agreement between the two sets of results is generally good, with most data points agreeing to within 10%, and the worst cases showing a 15% disparity. For charge 5, our cross sections are substantially larger than those reported in Ref. [16].

We have also included a comparison to fragment production cross sections from a 581 MeV/nucleon ^{22}Ne beam on a hydrogen target [18] (the same data were used to obtain σ_{cc} in [15]). For charges from 5 to 8, these results are in excellent agreement with the present experiment, but a substantial difference is seen in the charge 9 cross section. This is likely due in part to the increased number of fluorine isotopes that can be produced with ^{22}Ne ($A=20,21$), but it may also indicate dependence on the beam ion's isospin in the mechanisms that result in a one-unit charge change. If we subtract the 27 mb increase in the F production cross section from the charge-changing cross section reported in Ref. [15] and shown in Table II, we arrive at a value of 300±9 mb, which is (perhaps fortuitously) in excellent agreement with our measured value of 299±9 mb.

All fragment production cross sections increase with increasing target mass, as do the cross sections for pedestal events. In Fig. 7, we show, for each target except Ta, the fraction of the charge-changing cross section that goes into production of a particular fragment species. (The Ta data points have been excluded, as they are very close to those from the Pb target.) With the exception of the hydrogen target data, the data are tightly bunched and follow very similar patterns. For fragment charges from 6 to 9, as target mass increases, the fractions of the cross section going into a particular fragment species decrease, and this is also true for charge 5 with the exception of the hydrogen target. This is due to increased production of lighter fragments with heavier targets. The pattern suggests that, given an interaction, a larger target is likely to cause more catastrophic breakup of the projectile. The data also clearly show the enhancement of fragments with even Z compared to those with odd Z. This effect is well known and appears in several previously-reported measurements [7,16,18,19].

VI. COMPARISON OF THE CHARGE 5–9 CROSS SECTIONS TO MODEL CALCULATIONS

Table IV shows the measured fragment production cross sections, as in Table III, along with predictions from Nucfrg2 [13], the parametrization of Nilsen *et al.* [20], and the Qmsfrg model [21], for which we have results for the C, Al, and Cu targets. We begin by discussing the Nucfrg2 results.

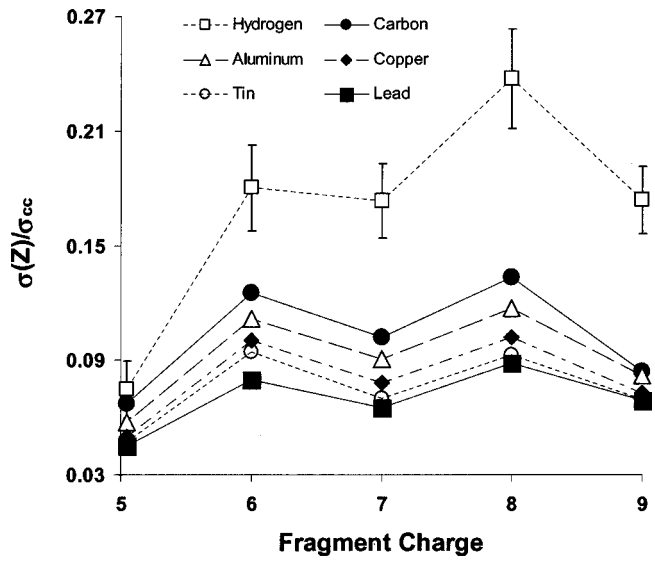

FIG. 7. Fragment production cross sections for charges 5–9, as fractions of the charge-changing cross sections for the different targets excluding Ta. The data show enhanced even-Z production, and the fractions decrease with increasing target mass. Uncertainties in the data are indicated by the size of the symbols, except in the case of the hydrogen target data where the error bars are shown explicitly.

For F production, the model predictions are consistently higher than the data, although the discrepancies decrease with increasing target mass. The model cross sections are in excellent agreement with the data for the production of O and N for the C and Al targets, but as target mass increases predicted cross sections fall below the data by as much as 33%. For C production, the model predictions are substantially below the data for all targets, typically by about 40%. Finally, for B, the model predictions for all targets are in fairly good agreement with the data, particularly for the lighter targets. For the combined $Z=1$ to 4 category, we are unable to make a meaningful comparison to Nucfrg2 because the output cross sections—unlike the cross sections we extract from the data—are weighted by the predicted fragment multiplicities. Because the average multiplicities of protons and helium ions are predicted to be greater than one per interaction, the weighting leads to summed production cross sections that are much greater than the charge-changing cross section for a given target material.

The parameters for the Nilsen *et al.* fit [20] were determined using data for beams (Kr, Ag) of much higher mass than Ne. In Ref. [7], we found that those parameters predicted fragment cross sections that agreed well with our data for charges from 12 to 25, although the enhancement of even-Z fragment production seen in those data was not reproduced. Here, the data in Table IV indicate that this set

TABLE IV. Charges 5 through 9 fragment cross sections in millibarns, compared to the Nucfrg2 [13] and Qmsfrg [21] models, and to the parametrization of Ref. [20].

Z_{frag}	σ (mb) from	H	C	Al	Cu	Sn	Ta	Pb
9	This expt.	52±4	83±4	111±5	144±7	177±9	215±10	235±11
	Nucfrg2	57	129	151	179	212	245	258
	Qmsfrg		93	117	134			
	Ref. [20]	100	150	178	216	251	280	289
8	This expt.	71±6	132±6	159±7	202±9	236±12	280±13	300±14
	Nucfrg2	70	135	160	181	200	216	221
	Qmsfrg		125	158	206			
	Ref. [20]	76	108	127	154	178	197	203
7	This expt.	52±5	101±4	123±6	155±7	178±9	213±10	221±11
	Nucfrg2	30	103	126	143	159	172	176
	Qmsfrg		96	121	131			
	Ref. [20]	57	89	104	126	145	160	166
6	This expt.	54±5	124±5	151±7	198±9	239±11	255±12	271±13
	Nucfrg2	38	85	107	122	137	148	152
	Qmsfrg		125	153	185			
	Ref. [20]	44	78	91	109	126	139	143
5	This expt.	22±4	66±3	78±4	99±7	120±7	144±10	153±10
	Nucfrg2	21	70	90	104	117	127	130
	Qmsfrg		58	66	54			
	Ref. [20]	33	70	82	98	112	124	128
1–4	This expt.	61±16	494±20	743±30	1167±48	1489±64	1914±86	1981±87
	Ref. [20]	69	300	270	322	371	408	420

TABLE V. Production cross sections in millibarns for the light fragment and pedestal event categories, using the d3mm3/4 and d3mm5/6 detector pairs. The ''charge 3'' and charge ''4'' categories both contain contributions from events where multiple lower-charged fragments are detected in coincidence, mimicking a signal of a single fragment with the nominal charge.

Z_{frag}	σ (mb) from	H	C	Al	Cu	Sn	Ta	Pb
6	d3mm1/2	54±5	124±5	151±7	198±9	239±11	255±12	271±13
	d3mm3/4	59±6	125±5	155±7	199±9	238±12	255±12	267±13
	d3mm5/6	56±6	123±5	149±7	191±9	225±11	233±11	237±12
	5/6 acc.	0.95	0.95	0.95	0.94	0.94	0.91	0.90
5	d3mm1/2	22±4	66±3	78±4	99±7	120±7	144±10	153±10
	d3mm3/4	16±3	64±3	69±5	94±5	110±7	126±8	134±7
	d3mm5/6	17±2	59±3	70±4	88±4	102±6	109±6	114±7
	5/6 acc.	0.90	0.90	0.90	0.89	0.89	0.86	0.86
''4''	d3mm3/4	18±4	71±4	82±5	105±6	124±16	115±9	134±7
	d3mm5/6	17±2	46±2	58±3	63±5	77±7	86±6	86±6
''3''	d3mm3/4	12±6	121±7	144±9	194±11	213±17	231±19	269±17
	d3mm5/6	19±4	95±5	117±9	153±8	168±10	196±16	216±12
Three He	d3mm3/4	31±5	73±6	89±7	107±8	112±11	177±12	151±12
	d3mm5/6	16±3	56±3	58±4	70±6	80±7	94±13	82±7
2	d3mm3/4	4±5	119±6	180±13	257±13	312±19	374±19	369±21
	d3mm5/6	12±5	129±6	171±9	238±11	290±15	346±19	341±17
1	d3mm3/4	1±5	77±5	160±24	308±64	386±82	576±155	523±130
	d3mm5/6	6±6	95±11	166±15	254±24	312±34	389±42	429±47
pedestal	d3mm3/4	0±5	25±7	81±24	246±65	480±84	659±158	842±135
	d3mm5/6	0±6	76±11	186±15	458±29	735±44	1082±60	1199±66

of parameters does not work particularly well for the Ne beam data.

In contrast to the above two models, the Qmsfrg model [21] predicts cross sections that are generally in excellent agreement with the data for the subset of points where calculations are available. For charges 6–9, most of the calculated cross sections are within the error on the data. The only disparity of more than 18% between the model and the data is for B production in the Cu target.

Both the Nucfrg2 model and the Nilsen *et al.* parametrization fail to reproduce some of the more interesting features of the data. Most notably, the data show a clear trend towards large production cross sections for even-Z fragments (O, C) compared to odd-Z fragments (F, N). In particular, F production in the data is suppressed compared to both calculations. Typically, the largest fragment-production cross sections are those for removal of a single charge, and that is predicted for Ne by these models, but the prediction is not borne out by the data. Qmsfrg, on the other hand, correctly predicts the suppression of F production and the enhancement of even-Z fragment cross sections.

VII. FRAGMENT PRODUCTION CROSS SECTIONS IN THE 1 TO 4 RANGE

As shown in Figs. 4(b) and 4(c), light fragment peaks emerge in the d3mm3/4 and d3mm5/6 analyses, and are particularly clear in the Z_{56} spectra. Using the same methods as were applied to the Z_{12} spectra, we can extract charge-changing and production cross sections for all fragment species. In the d3mm1/2 analysis, events with Z_{12} from about 0.5 to 4.8 were grouped into a single category. With the improved resolution of light fragment events at small acceptance, we can count events in the following categories: (1) Charge 1, with Z from 0.5 to about 1.75—some data sets show distinct peaks around 1.7, consistent with three protons detected in coincidence; (2) Charge 2, including the entire broad peak corresponding to He and He plus one or more protons; (3) ''Charge 3,'' which contains events with one Li or two He fragments, which cannot be cleanly separated from one another in these data; (4) Three-He, corresponding to the events in the peaks around 3.5 in Z; (5) ''Charge 4,'' discussed in detail below.

As in the d3mm1/2 analysis, the charge 5 and 6 categories include events where at least one light fragment is present in coincidence with the leading fragment. Events with $Z<0.5$ are, as before, counted as pedestals. Cross sections for the categories listed above and for charges 5 and 6 are shown in Table V. The uncertainties include contributions added in quadrature from the 4% systematic error described above, counting statistics, and the uncertainties associated with the assignment of bins to charge categories [24]. The latter are larger in the d3mm3/4 analysis than in d3mm5/6, due to the

comparatively large numbers of events present in the valleys between peaks. The very low end of the spectrum typically contains several hundred events in the region of Z from about 0.2 to 0.5. These are treated as pedestal events, but, because their source is unclear [25], we include them in the uncertainties for both $Z=1$ and pedestals. This accounts for the comparatively large errors on those data points, particularly in d3mm3/4.

Charge-changing and fragment production cross sections for charges 7 through 9 in d3mm3/4 and 5/6 were also obtained. Within the statistical and systematic uncertainties, results from the downstream detector pairs are consistent with those from d3mm1/2, after a small normalization correction (accounting for lost Ne events) is applied. The corrections bring the charge-changing cross sections in d3mm3/4 and d3mm5/6 into agreement with those measured in d3mm1/2.

The charge 5 and 6 cross sections—including those in d3mm1/2—are shown in Table V because, unlike the charge 7 to 9 cross sections, there are some significant decreases in the more-downstream detectors. The decreases are largest for the heavier targets, in qualitative agreement with Ref. [23], where the width parameter σ_0 is predicted to depend slightly on the target's atomic number. (This amounts to 5% in going from a carbon target to a lead target in the present experiment.) The predicted acceptances for charges 5 and 6 in d3mm5/6 are shown in Table V, with σ_0 fixed at 100 MeV/cycles for all targets. A larger value of σ_0 would give model predictions for charge 5 in slightly better agreement with the data, but the agreement for charge 6 would be worse.

The mixture of states that contributes to the ''charge 4'' peak precludes a simple leading-fragment interpretation of the decrease in cross sections that is seen in comparing the d3mm5/6 result to d3mm3/4. In the acceptance model, using $\sigma_0 = 100\,\mathrm{MeV}/c$ for all targets, the predicted ratio of the cross sections in d3mm5/6 to that in d3mm3/4 is in the range 73–87 %, depending on the target and Be isotope. The weighted average of the ratio of the d3mm3/4 to d3mm5/6 cross sections is 0.68 ± 0.02, a steeper falloff than predicted, even if (somehow) only ^{7}Be were produced. This is indirect evidence that the ''charge 4'' state has a significant contribution from events with combinations of lighter fragments producing a signal equivalent to that of a Be fragment; direct evidence is shown in Sec. VIII, where we use data from Scint2 to greatly improve the reliability of the Be cross sections.

The cross sections for three He fragments in coincidence decrease in d3mm5/6 compared to d3mm3/4. The explanation is simple: If one of the fragments misses d3mm5/6, the event will count as ''charge 3,'' and if two are outside, the event will be recorded as charge 2. This feed down also explains, in part, why cross sections for charges 1 and 2 show little or no decrease when we compare the d3mm5/6 results to d3mm3/4: while some protons and He fragments are lost, other events go into these categories when heavier fragments are lost. The most notable shift is to pedestal events, for which the cross sections increase markedly as acceptance decreases.

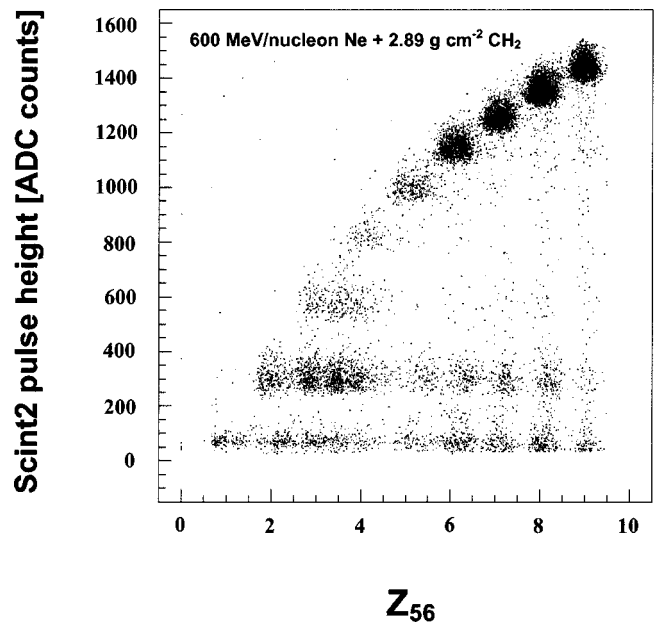

FIG. 8. Scatter plot of pulse height in Scint2 vs Z_{56}, used to disentangle some of the contributions to low-Z events. Polyethylene target data.

VIII. CORRELATION OF SIGNALS IN d3mm5/6 AND Scint2

To extend the analysis beyond the particle identification capabilities of the silicon detectors, in Fig. 8 we plot the pulse height in the far-downstream plastic scintillator (Scint2) vs the Z_{56} value, with an event sample (with the CH_2 target) that excludes events with Ne ions and events in which Scint2 had no hit. Because Scint2 subtended a small acceptance angle (about 0.5°), its spectra are strongly influenced by the fragment angular distributions and multiplicities, which helps clarify some types of light-fragment events.

Before discussing specific fragment combinations, we note that the fraction of pedestal events (no charged particles seen) in Scint2 increases monotonically with increasing target mass, from about 20% in the target-out runs, to about 35% for the lightest targets (C, CH_2, Al), reaching about 70% for Ta and Pb; this is due to Coulomb multiple scattering in the targets. The widths of angular distributions depend approximately linearly on target Z [26]. Comparing the fraction of Ne ions that are detected in Scint2 to predictions from the acceptance model, the agreement is better than 5% for all targets except Cu, where a 10% discrepancy is seen. The calculations used a beam divergence of 2.2 mrad, chosen to reproduce the measured acceptance of Ne in Scint2 in the target-out data.

The four densely populated clusters of events in the upper right-hand corner of Fig. 8 correspond to charges 9, 8, 7, and 6, as indicated by the Z_{56} values. There are also obvious clusters of events with a pulse height of about 300 counts in Scint2, which are events where only a single He fragment hit Scint2. These clusters are distinctly visible at Z_{56} values of (approximately) 2, 3, 3.5, and 4, 5.5, etc. Many single-He events are seen on events with Z_{56} in the range 5–8, consistent with our interpretation of the secondary peaks seen slightly above integer values associated with charges 5 and

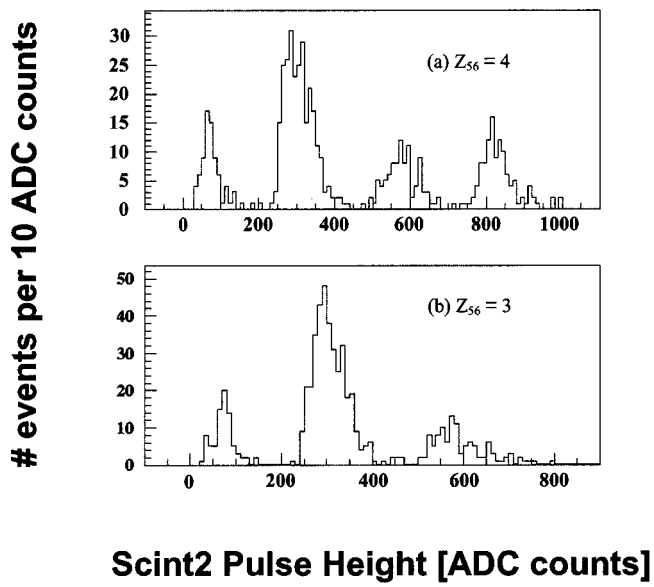

FIG. 9. Histograms of Scint2 pulse height for events with $Z_{56}=4$ [upper plot, (a)], and for events with $Z_{56}=3$ [lower, (b)]. In both categories, only a single He fragment (pulse height around 300 counts) is seen in the scintillator on a high percentage of events [49% in (a), 61% in (b)].

6. Most often Scint2 is hit by the heavier fragment, but occasionally the heavier fragment misses and only the accompanying He fragment hits. Figure 8 also shows a band of events for $Z_{56}=5$ to 8 in which Scint2 is hit only by one or two H fragments; there, again, the heavier fragments miss Scint2, but the H fragments do not.

Figure 8 illustrates the difficulties associated with extracting cross sections for the ''charge 4'' and (especially) ''charge 3'' states. Though we presented a single cross section for these categories in Table V, there are undoubtedly contributions coming from events that do not include the presumed leading fragment. Considering the charge 4 case, in Fig. 9(a) we take events around $Z_{56}=4$ and histogram the pulse height in Scint2. We find that, for various targets, 20–40 % of the events in the histogram are consistent with a Be fragment in Scint2, 10–20 % are consistent with one Li or two He, 35–50 % have a single He, and 10–20 % have a H fragment. This suggests that the ''charge 4'' peak in the Z_{56} spectrum is actually dominated by events with four or five He fragments, or with an Li fragment in coincidence with either a He fragment or a second Li fragment. The relationship between detected Z and actual Z as per equation (2) shows that any of those combinations would mimic a Be or (Be+He) signal in a silicon detector. Taking a similar histogram of Scint2 pulse height for events around $Z_{56}=3$ yields the histogram shown in Fig. 9(b), where only 20–30 % of the events are consistent with Li or two He in Scint2, 60–65 % show a single He fragment, and 10–15 % show a H fragment. It seems likely that this event category is dominated by two-He events.

Figure 8 also shows a dense cluster of events with a single He fragment hitting Scint2 and with $Z_{56}\approx 3.5$, consistent with our interpretation of that peak as being due to the detection of three He fragments in coincidence. Taking a slice around this Z_{56}, and projecting onto the Scint2 axis, we find that typically about 60% of the Scint2 hits correspond to a single He fragment, about 20% correspond to two He fragments (or, conceivably, one Li fragment), and 15–20 % are due to a single H fragment. A very small fraction of events, between 1% and 3% of the total, are consistent with all three He fragments hitting Scint2.

TABLE VI. Percentages of events in various categories as seen in d3mm5/6 (2.6° acceptance) and in Scint2 (0.5° acceptance).

Z_{56}	%ev w/H in Scint2	%ev w/He in Scint2	%ev w/Li or 2 He in Scint2	%ev w/Be or equiv in Scint2
''4''	14±5	41±5	15±5	30±7
Three He	14±3	62±2	22±3	
''3''	21±3	61±2	18±2	
2	33±4	67±4		

In Table VI, we show the species of fragment identified in Scint2 for four categories of events as seen in d3mm5/6. The categories are ''charge 4,'' three-He, ''charge 3,'' and charge 2. The fractions in the various categories appear–within the low statistics in this data set–to be independent of the target. Accordingly, data from all targets have been combined in the table to produce averages and rms deviations for the various categories. These averages for Li(18±2%) and Be(30±7%) in Scint2 can be combined with the ''charge 3''and ''charge 4'' cross sections in Table V and corrected for acceptance, giving upper limits on the production of Li and Be, respectively.

IX. Be, Li, AND He PRODUCTION CROSS SECTIONS USING Scint2

The observed Scint2 spectra are useful in extracting the fragment cross sections, particularly for Be production. Consider an event with a Be signal in d3mm5/6. If the Scint2 pulse height is also consistent with Be, there are two possibilities: first, that there was a/Be fragment in the event and it hit Scint2; second, that the same (or nearly the same) combination of fragments that hit d3mm5/6 also hit Scint2. A simple argument shows that the events with a Be fragment comprise the vast majority of these events. If a Be-like signal in d3mm5/6 is produced by a combination of lighter fragments, the probability that all of them also hit Scint2 is much smaller than the probability that a Be ion in d3mm5/6 would hit Scint2. Acceptance calculations show that the probability of a ^{4}He fragment produced in the target reaching Scint2 is in the range 5–12 %, depending on the target and the assumed value of σ_0, whereas the corresponding probabilities for ^{9}Be are in the range 10–21 %. In, for example, an event where four He fragments produce $Z_{56}\approx 4$, assuming their production angles are not mutually correlated, the probability of all four hitting Scint2 is on the order of 10^{-4}, about three orders of magnitude lower than that for a Be fragment to hit Scint2. Correlated ^{4}He production angles increase the probability for all the He fragments in an event to hit Scint2, but the probability remains much smaller than that for Be to hit

TABLE VII. Upper limits on cross sections for BE and Li production, in millibarns, along with adjusted cross sections for the production of He as the leading fragment. The Be upper limits are likely very close to the true production cross sections, as explained in the text. Model predictions from Nucfrg2 and Ref. [20] are also shown.

Z_{frag}	σ (mb) from	H	C	Al	Cu	Sn	Ta	Pb
4	This expt.	8 ± 3	21 ± 6	26 ± 8	29 ± 8	35 ± 10	39 ± 11	39 ± 11
	Nucfrg2	18	34	45	52	59	64	66
	Ref. [20]	24	65	76	90	104	114	119
3	This expt.	$\leqslant6\pm1$	$\leqslant30\pm5$	$\leqslant37\pm7$	$\leqslant48\pm9$	$\leqslant53\pm10$	$\leqslant62\pm12$	$\leqslant68\pm12$
	Nucfrg2	11	49	66	77	87	95	98
	Ref. [20]	18	60	70	84	96	105	109
2	This expt.	59 ± 15	321 ± 34	440 ± 45	589 ± 56	684 ± 65	856 ± 100	836 ± 80
	Nucfrg2	226	654	727	788	846	913	937
	Ref. [20]	13	56	66	78	90	98	102

Scint2, by roughly an order of magnitude. We conclude that the ''charge 4'' peak in Scint2 is indeed dominated by events with a Be fragment, and that contamination from events with combinations of lighter fragments is less than 20% and likely smaller [27,28].

The analogous argument using the Scint2 pulse height for the $Z_{56}\approx3$ events (with one Li or two He fragments) does not yield a similarly clear conclusion, because a pair of ^{4}He ions created by decay of ^{8}Be will have a slightly larger acceptance than that of ^{6}Li or ^{7}Li. On the other hand, if two ^{4}He ions are produced with uncorrelated production angles, the probability for detecting both in Scint2 is 10–20 times lower than that for detecting a single ^{6}Li fragment. There is no way to infer whether a ''charge 3'' hit in Scint2 was more likely from a Li ion or a pair of He ions, so that we can only quote upper limits on Li production.

Table VII shows the upper limits on the Li cross sections, and also Be cross sections that differ substantially from the ''charge 4'' cross sections shown in Table V [29]. Compared to the d3mm5/6 results, the Li cross section upper limits are smaller than the ''charge 3'' cross sections by about factor of 3, and the Be cross sections are smaller than ''charge 4'' cross sections by about a factor of 2. These reductions account for the many events that appear in the ostensible Li or Be peaks but are in fact due to multiple light fragments. The $\leqslant$20% contamination of the Be samples, described above, is in every case smaller than the uncertainties already accounted for.

Also shown in Table VII are adjusted cross sections for He production; since we attribute large fractions of the ''charge 3'' and ''charge 4'' cross sections in d3mm5/6 to events where the leading fragment is actually He, it is appropriate to add these contributions to the other cross sections where the leading particle is clearly He (''three He'' and $Z_{34}=2$). We have used d3mm3/4 cross sections, since the acceptance for ^{4}He is much larger there ($\approx$75%) than in d3mm5/6 ($\approx$55%). Some of the Li cross sections in Table VII are from events with two He fragments; if properly identified, these would increase the He cross sections. However, even if 100% of those were due to two-He events, they would only increase the He cross sections by $\leqslant$10%; the uncertainties have therefore been increased to reflect this possibility, by adding the upper limits on the Li cross sections in quadrature with the previously tabulated He uncertainties.

Table VII also shows the predicted fragment production cross sections from Nucfrg2 and the parametrization of Ref. [20]. For charges 3 and 4, the Nucfrg2 cross sections are typically 50–100 % above the data (upper limits for Li), and the Ref. [20] model predicts cross sections that are even larger. For the He cross sections, even though the Nucfrg2 cross sections are enhanced by multiplicity weighting, they are within about a factor of 2 of the data for all but the H target, and within 12% for the two heaviest targets. In contrast, the Ref. [20] model predicts cross sections that are nearly an order of magnitude smaller than the measured values. Because these models depend on input from experimental data, it is likely that the large disparities seen here are due (at least in part) to the lack of previous data on light fragment cross sections.

X. CONCLUSIONS

Charge-changing cross sections for interactions of ^{20}Ne ions at 600 MeV/nucleon on several elemental targets have been extracted and are seen to agree, typically to 3% or better, with the predictions of geometric models. Fragment production cross sections near the beam axis have also been extracted, for charges 5–9 using data from detectors with large acceptance (7°) where acceptance for these species is expected to be >99%, and for lighter fragments using smaller-acceptance detectors. The fragment production cross sections for charges 5–9 show a strong enhancement for production of even-Z ions, and two models [13,20] that agreed well in earlier comparisons to Fe beam data do not accurately reproduce the Ne data, whereas the more recent Qmsfrg, which incorporates quantum effects [21], does quite well in reproducing many details of the data, including the even-Z enhancements. Multiple fragment states seen in the silicon detectors have been disentangled, to the extent pos-

sible, using the downstream scintillator with a 0.5° acceptance angle. This allows us to quote upper limits on the production cross sections for Be and Li, with the Be upper limits expected to be very close to the actual cross sections, and to improve our estimates of the production cross sections for leading-He events. The light-fragment production cross sections have not been previously measured. Where possible, these have been compared to models, and the Nucfrg2 code is seen to give results that are more compatible with the data than are the results from the parametrization of Nilsen *et al.* The latter has particular problems for He, predicting cross sections that are nearly an order of magnitude smaller than the measured values. Neither model does well in predicting the Li and Be cross sections, and overall the models are much less accurate for this beam than they are for heavier beams such as Fe.

ACKNOWLEDGMENTS

We gratefully acknowledge the tremendous efforts of the HIMAC accelerator operators, in particular Dr. E. Takada, for providing us with excellent beams and stable conditions in this and other runs. This work was supported at LBNL, by the Space Radiation Health Program of the National Aeronautics and Space Administration under NASA Grant Nos. L14230C and H31909D, through the U.S. Department of Energy under Contract No. DE-AC03076SF00098. At HIMAC, this work was supported in part by the Research Project with Heavy Ions at NIRS-HIMAC, Project No. 9P037. One of us (J.M.) acknowledges travel support from the Japan Society for the Promotion of Science (JSPS).

APPENDIX: A THREE-DIMENSIONAL MONTE CARLO ACCEPTANCE SIMULATION

We make extensive use of our Monte Carlo acceptance model in interpreting variations in spectra produced by the different detector pairs. Here, we describe the code and many of its details. It is sufficiently general that it can be applied to many beamline arrangements; specific setups corresponding to our experiments are written into the code, but it can also read a beamline setup file (in a particular format), in order to have wider applicability.

We define the acceptance angle of a detector to be the half-angle of the forward cone it subtends, as seen from a point on the beam centerline at the middle of the target. In a fragmentation event in which multiple fragments are produced, all at or near the beam velocity, a silicon detector signal will be proportional to the total charge liberated by all the fragments that hit it. Assuming that all fragments are at equal velocity (βc), the observed Z_{eff} is given by

$$-\frac{dE}{dx}=-\sum_i\left(\frac{dE}{dx}\right)_i=f(\beta,Z_{\mathrm{mat}})\sum_i Z_i^2=f(\beta,Z_{\mathrm{mat}})Z_{\mathrm{eff}}^2, \tag{A1}$$

where the sums run over all fragments, and functional form of the Bethe-Bloch equation for singly-charged particles is represented by *f*. To first order *f* depends only on β and the material being traversed. The presence of a ''heavy'' leading fragment—one with charge not too far from the beam charge—causes the sum in equation (A1), and hence the signal from a silicon detector, to be dominated by that fragment's *Z*.

The spectra shown in Figs. 4(a)–4(c) illustrate the effect of acceptance on measured spectra. In this and similar experiments, detectors at large acceptance show obvious fragment peaks down to about half the charge of the beam ion, below which the spectra become indistinct. At small acceptance, many more peaks are visible. The smearing of large-acceptance spectra at lower fragment charges is due to combinatorial effects: when only light fragments are produced, many combinations can lead to a particular value of energy loss in the detector, hence no distinct peaks are seen. Small-acceptance detectors show peaks for all fragment species because some light fragments miss these detectors on high-multiplicity events, an effect illustrated by Fig. 5, where bands of events can be seen in which one or more particles hitting the upstream detector missed the downstream detector.

In calculating cross sections for a particular fragment species, we are integrating the true (and *a priori* unknown) angular distribution of the fragment's parent distribution over the angular acceptance of the detector. For a given beam charge *Z*, mass *A*, and kinetic energy *E*, and a particular fragment Z_f and A_f, we can write

$$\sigma_{\mathrm{measured}}(Z,A,E,Z_f,A_f,\theta_d)=\int_0^{\theta\pi}d\phi\int_0^{\phi_d}\frac{d\sigma}{d\theta}d\theta, \tag{A2}$$

where θ_d is the acceptance angle, as defined above, of a particular detector, and the differential cross section $d\sigma/d\theta$ depends on the same set of variables as $\sigma_{\mathrm{measured}}$. We assume azimuthal symmetry, making the integration over ϕ trivial. When $\theta_d\rightarrow\pi$, the measured cross section approaches the true total production cross section for the given isotope. We define the acceptance, or efficiency of detection, as the ratio of the measured cross section to the true, i.e.,

$$\varepsilon_{\mathrm{det}}(Z,A,E,Z_f,A_f,\theta_d)=\sigma_{\mathrm{measured}}/\sigma_{\mathrm{true}}. \tag{A3}$$

Since isotopes of a given species are not identified separately, we average over the acceptances of 2–3 of the most abundant naturally-occurring isotopes of a given species. This introduces an inherent uncertainty in the corrections, although in many cases (typically when it is near 1) $\varepsilon_{\mathrm{det}}$ varies by only a few percent over the range of A_f being considered.

For the beam energies considered here and in other similar data sets we have obtained (290 to 1200 MeV/nucleon), nuclear interactions are the most important source of fragments produced at ''large'' angles relative to the beam direction. Coulomb multiple scattering in the target (particularly when high-*Z* materials such as lead are used) and in the detector stack are also relevant, as are the finite size and angular divergence of the incident beam. In our simulation, the beam parameters are specified by the user at run time, as

is the run number (which is a convenient way of specifying the target and the detector configuration). For almost all of our data sets, information from PSD's allows us to accurately specify the beam size and shape in the simulation. It is usually possible to find an internal consistency check to find the beam divergence angle; in the present experiment, the acceptance of Ne ions in Scint2 in target-out data provided the check.

To simulate the dynamics of nuclear interactions, we rely on the statistical model of fragmentation first proposed by Goldhaber [10], in which (in the rest frame of a projectile with mass number A_p), the momentum p_i of the outgoing fragment (mass A_f) in any Cartesian coordinate i is normally distributed with a width given by

$$\sigma_{p_i}^2 = \sigma_0^2 A_p (A_p - A_f)/(A_p - 1). \tag{A4}$$

More recently, Tripathi and Townsend [23] surveyed the published experimental data on fragment angular distributions and showed that the existing data are fit well by a parametrization of σ_0 that incorporates Coulomb effects in the nuclear interaction and therefore depends on the beam energy and the charges of both projectile and target. For each simulated run, this parametrization is used to calculate a nominal σ_0, which can be modified by the user before the simulation proceeds. Varying σ_0 allows us to find the empirical values that best reproduce the data. We assume that the relativistic boost is purely along the nominal beam axis, so that the transverse momentum of the fragment in the rest frame of the projectile is also transverse in the laboratory. The strong dependence on the magnitude of the boost results in angular distributions in the laboratory frame that vary considerably with beam energy.

During initialization of the simulation program, the user is queried as to whether a particular run is to be simulated. If so, the run number requested selects the configuration of detectors, and points to a database file of targets (indexed by run number), so that the simulation includes all elements on the beamline with a minimum of manual input. Given the beamline configuration, the Monte Carlo routine loops over ion species, starting with the primary and ending with protons. Because the experimental data lack isotopic resolution, production of the two or three most naturally abundant isotopes of each species is simulated and the results for each isotope are tabulated separately. The program generates 10^4 events per isotope. An event in the simulation begins by throwing the depth of the interaction in the target, based on the simple exponential form, $\exp(-x/\lambda)$, that describes the survival of the primary ion. The mean free path for a charge-changing nuclear interaction, λ, depends in part on the cross section; we use a simple geometrical model [12] for those. The primary's starting position at the target entrance is calculated based on the beam parameters specified by the user. The position at the interaction depth is calculated with a straight-line trajectory, which is modified according to the (Gaussian) Coulomb multiple scattering recipe of Ref. [25], using a modified Molière formula [26] to describe the width of the scattering distribution. The multiple scattering algorithm yields both the accumulated transverse deflection of the primary ion and the accumulated change in its angle with respect to the beam axis. These become the starting position and momentum vectors for the outgoing fragment. The trajectory of the fragment is further modified by adding the contribution from nuclear scattering, which also has a normal angular distribution with width given by equation (A4). The fragment is followed along the given trajectory to the target exit, where its position and trajectory are again modified by Coulomb scattering.

The fragment's momentum vector at the target exit is used to define a straight-line trajectory through the air gap to the first detector downstream of the target. At the detector, the distance from the beam axis is calculated and, if it is smaller than the detector's radius, the hit counter is incremented. The position and momentum of the fragment are again modified by Coulomb multiple scattering in the silicon detector, and this information is used to calculate the position at the next detector, and the procedure is repeated. The fragment is followed through the entire detector stack in this manner, and then the process is repeated until all 10^4 trials have been performed for the particular isotope. The acceptance for a given detector and isotope is simply the number of hits in the detector divided by the number of trials. When all acceptances have been computed, the results are output to disk in a text file. For the primary ion, at the energies encountered in our experiments, the acceptance is always close to 100% except in detectors with very small ($<1°$) acceptance, and/or when heavy targets are simulated. Fragment acceptances decrease monotonically with decreasing mass, and with decreasing beam energy, as expected.

[1] S. B. Curtis, L. W. Townsend, and J. W. Wilson, Trans. Am. Nucl. Soc. **64**, 462 (1991).

[2] J. R. Castro, in *Cancer Management in Man*, edited by A. L. Goldson (Kluwer Academic, Dordrecht, The Netherlands, 1989), pp. 179–182.

[3] National Research Council, Task Group on the Biological Effects of Space Radiation, *Radiation Hazards to Crews of Interplanetary Missions—Biological Issues and Research Strategies* (National Academy, Washington, D.C., 1996).

[4] J. A. Simpson, in *Composition and Origin of Cosmic Rays*, edited by M. M. Shapiro (Reidel, Dordrecht, 1983), p. 1.

[5] J. W. Wilson, M. Kim, W. Schimmerling, F. F. Badavi, S. A. Thibeault, F. A. Cucinotta, J. L. Shinn, and R. Kiefer, Health Phys. **68**, 50 (1995).

[6] C. Zeitlin, J. Miller, L. Heilbronn, K. Frankel, W. Gong, and W. Schimmerling, Radiat. Res. **145**, 655 (1995).

[7] C. Zeitlin, L. Heilbronn, J. Miller, S. E. Rademacher, T. Borak, T. R. Carter, K. A. Frankel, W. Schimmerling, and C. E. Stronach, Phys. Rev. C **56**, 388 (1997).

[8] C. J. Zeitlin, K. A. Frankel, W. Gong, L. Heilbronn, E. J. Lampo, R. Leres, J. Miller, and W. Schimmerling, Radiat. Meas. **23**, 65 (1994).

[9] M. Wong, W. Schimmerling, M. H. Phillips, B. A. Ludewigt, D. A. Landis, J. T. Walton, and S. B. Curtis, Med. Phys. **17**, 163 (1990).
[10] A. S. Goldhaber, Phys. Lett. **53B**, 306 (1974).
[11] R. Brun, O. Couet, C. E. Vandoni, and P. Zanarini, Comput. Phys. Commun. **16**, 147 (1989).
[12] L. W. Townsend and J. W. Wilson, Radiat. Res. **106**, 283 (1986).
[13] J. W. Wilson, J. L. Shinn, L. W. Townsend, R. K. Tripathi, F. F. Badavi, and S. Y. Chun, Nucl. Instrum. Methods Phys. Res. B **94**, 95 (1994).
[14] H. C. Bradt and B. Peters, Phys. Rev. **77**, 54 (1950).
[15] C.-X. Chen *et al.*, Phys. Rev. C **49**, 3200 (1994).
[16] W. R. Webber, J. C. Kish, and D. A. Schrier, Phys. Rev. C **41**, 533 (1990).
[17] A. Fukumra, T. Hiraoka, T. Tomitani, T. Kanai, T. Murakami, S. Minohara, N. Matsufuji, H. Tomura, Y. Futami, T. Kohno, and T. Nakamura, JAERI-Conf 96-008, Proceedings of the 1995 Symposium on Nuclear Data, 1996, p. 248.
[18] C. N. Knott *et al.*, Phys. Rev. C **53**, 347 (1996).
[19] J. R. Cummings *et al.*, Phys. Rev. C **42**, 2508 (1990).
[20] B. S. Nilsen, C. J. Waddington, J. R. Cummings, T. L. Garrard, and J. Klarmann, Phys. Rev. C **52**, 3277 (1995).
[21] F. A. Cucinotta, J. W. Wilson, R. K. Tripathi, and L. W. Townsend, Adv. Space Res. **22**, 533 (1998).
[22] F. James and M. Roos, Comput. Phys. Commun. **10**, 343 (1975).
[23] R. K. Tripathi and L. W. Townsend, Phys. Rev. C **49**, 2237 (1994).
[24] In attempting to determine the number of events in various light-fragment categories, we have performed multiple-Gaussian fits to each Z spectrum using MINUIT [22] from within PAW. The fits are sensitive to the chosen starting parameters and the choice of which bins to fit for a particular peak; the results are, with some choices, clearly erroneous. The difficulties are due at least in part to the fact that many of the peaks are not well described by Gaussians. This, in turn, is probably related to the fact that several combinations of light fragments can produce peaks with similar, but not exactly identical, Z_{eff}, resulting in complicated substructures around the various peaks. Also, the fit errors returned by MINUIT are inflated, since there is strong correlation between the parameters for neighboring peaks. Because of the generally unsatisfactory results obtained by peak fitting, we have opted to sum over what we believe are the appropriate bins corresponding to the various event categories, and to take into account the uncertainties arising from the slightly subjective process of choosing bins.
[25] The nature of the events that appear with Z between about 0.2 and 0.5 in d3mm3/4 or d3mm5/6 is uncertain. An event with a single proton that hits, for example, d3mm3 but misses d3mm4 would deposit half the nominal proton ΔE_{34}, and would appear near $Z_{34} \approx 0.7$, significantly larger than the observed Z's. Using the high-gain channels does not help; the majority (50–85 %) of these events appear as pedestals, which is why we count them as pedestals, but some (10–30 %) appear as protons, and the rest still appear between 0.2–0.5 in Z. Nothing unusual is seen in examining the x and y position distributions for these events, ruling out the possibility that they are due to hits at the edges of the detectors. An increasing fraction of events falls into this category as the target mass increases.
[26] G. Lynch and O. Dahl, Nucl. Instrum. Methods Phys. Res. B **58**, 6 (1991). We use the Molière form defined by equations (1), (2), and (7).
[27] Particle Data Group, D. E. Groom *et al.*, Eur. Phys. J. C **15**, 1 (2000).
[28] Consider a possible reaction that produces two ^{8}Be fragments in the target, each of which decays to two ^{4}He nuclei; to a good approximation, each pair of He ions conserves the momentum of the ^{8}Be. The acceptance of each pair of He is almost exactly the same as that for the ^{8}Be had it not decayed, so the acceptance for all four He ions is approximately the square of the acceptance for a single Be ion, and this is still a factor of 5–10 smaller than the acceptance for either ^{7}Be or ^{9}Be. Thus even in the worst-case scenario—that 100% of the two-He events that are misidentified as Be arise from the decay of ^{8}Be—the contamination of the true Be sample can be no worse than 20%. It seems likely that the actual contamination is in fact smaller than this.
[29] The values in Table VII were arrived at as follows. The Be cross section upper limits are $35 \pm 8\%$ of the values in Table V (the fraction of Be in Scint2, excluding events with only a charge 1 fragment in Scint2), with additional corrections for acceptance in d3mm5/6 ($80 \pm 10\%$) and for losses due to charge-changing interactions of Be in the scintillators (4.4%). Similarly, Li cross section upper limits are $23 \pm 2\%$ of the values in Table IV, corrected for acceptance in d3mm5/6 ($75 \pm 9\%$) and for losses in the scintillators (3.9%). The acceptance uncertainties correspond to reasonable variations in isotope mass number and σ_0. The uncertainties shown in Table VII are the quadrature sums of the contributions from acceptance, the factors in Table VI, and the uncertainties on the cross sections in Table V.